HAL open science

CFD/DEM coupled approach for the stability of caisson-type breakwater subjected to violent wave impact

Dong Ding, Abdellatif Ouahsine, Weixuan Xiao, Peng Du

To cite this version:

Dong Ding, Abdellatif Ouahsine, Weixuan Xiao, Peng Du. CFD/DEM coupled approach for the stability of caisson-type breakwater subjected to violent wave impact. Ocean Engineering, 2021, 223, pp.108651. 10.1016/j.oceaneng.2021.108651 . hal-03363615

HAL Id: hal-03363615

https://hal.utc.fr/hal-03363615

Submitted on 13 Feb 2023

HAL is a multi-disciplinary open access archive for the deposit and dissemination of scientific research documents, whether they are published or not. The documents may come from teaching and research institutions in France or abroad, or from public or private research centers.

L'archive ouverte pluridisciplinaire **HAL**, est destinée au dépôt et à la diffusion de documents scientifiques de niveau recherche, publiés ou non, émanant des établissements d'enseignement et de recherche français ou étrangers, des laboratoires publics ou privés.

Distributed under a Creative Commons Attribution - NonCommercial 4.0 International License

Version of Record: https://www.sciencedirect.com/science/article/pii/S002980182100086X
Manuscript_c2dde69ddf8ac60ca2c7bb594b8be3a0

CFD/DEM coupled approach for the stability of caisson-type breakwater subjected to violent wave impact

Dong Ding[a], Abdellatif Ouahsine[a,*], Weixuan Xiao[b], Peng Du[c]

[a] *Sorbonne Universités, Université de Technologie de Compiègne, Laboratoire Roberval Centre de recherches Royallieu, CS 60319, 60203 Compiègne cedex, France*

[b] *Université Clermont Auvergne, CNRS, LIMOS, F-63000 Clermont-Ferrand, France*

[c] *School of Marine Science and Technology, Northwestern Polytechnical University, Xi'an 710072, China*

Abstract

Wave impacts on vertical caissons may cause breakwaters failures. This paper focuses on the analysis of the stability of breakwaters under violent wave impacts by using a triple-coupled Fluid-Porous-Solid model. The fluid model is described by the Volume-Averaged Reynolds-Averaged Navier-Stokes equations in which the nonlinear Forchheimer equations for the porous medium are added to the inertia terms. The solid model, based on the DDA method which is an implicit DEM method, has been used to analyze the movement and the stability of the caisson and armour units by taking into account the shapes of the armor units, as well as the contact between blocks. The developed model has been used for multiple purposes. Firstly, to estimate the variation of the maximum height of the impacting wave with the breakwater slope. A new formula has then been established for this purpose. Secondly, to analyze the influence of the porosity and of the thickness of the porous layer on the Turbulence Kinetic Energy (TKE) distribution around the breakwater structure. The results show that the higher the thickness, the lower the TKE intensity will be. Finally, the model has been used to analyze the stability of shaped armour units placed behind the caisson.

Keywords: Breakwater stability, Violent wave impacts, Fluid-Porous model, CFD/DEM coupling

1. Introduction

Breakwaters are used for the protection of harbors and beaches against wave action. Their failure may be caused by the motion of the caissons and the global instability of the rubble mound (Oumeraci (1994); Takahashi et al. (2001)). For the motion of caissons, the most common forms are sliding, subsidence, and overturning (Takahashi et al. (2014)), which may induce the movement of armour units to increase the failure of the breakwater.

Elsewhere, breakwater failures have been investigated by several empirical studies (Cuomo et al. (2010); Doan et al. (2020)) and by some numerical and experimental methods (Elchahal et al. (2008); Hofland et al. (2010)). For the computational techniques, the computational fluid dynamics (CFD) method is the most common tool used to describe the wave impacts. Kocaman and Ozmen-Cagatay (2015) discussed the impact of dam-break induced shock waves on a vertical wall by a CFD RANS-VOF solution. The simulation results show that the impact of dam-break flood waves on the vertical wall causes wave reflection against the wall

*Corresponding author
Email address: ouahsine@utc.fr (Abdellatif Ouahsine)

© 2021 published by Elsevier. This manuscript is made available under the CC BY NC user license
https://creativecommons.org/licenses/by-nc/4.0/

and the occurrence of a negative wave. The impacts of waves on the vertical wall were also investigated by Liu et al. (2019) using a two-phase compressible CFD solver. Recently, many researchers made a series of attempts to couple the fluid and solid models. Discrete Element Method (DEM) is usually used to calculate the movement of armour units. A wave-structure interaction method was proposed by Latham et al. (2009). In this method, the forces and the volume fraction from the CFD model are mapped onto the DEM structure. Ren et al. (2014) used a coupled SPH-DEM method to investigate the stability of armour units in rubble-mound breakwaters. An interfacial force-balance condition achieved the coupling between the fluid particle (SPH) and the solid spheres (DEM).

Due to the complexity of the breakwater structure, the porous medium should also be considered. Traditionally, Darcy's law and Forchheimer law were used to investigate linear and non-linear structures for porous armour layer (Whitaker (1996)). Hsu et al. (2002) proposed a mathematical model based on the Volume-Averaged Reynolds-Averaged Navier-Stokes (RANS) equations that coupled the fluid and the porous medium to describe surface wave motions in the vicinity of a coastal structure. In this model, the Forchheimer law was adds by the volume-averaged process. Additionally, this fluid and porous medium coupled model are also developed in OpenFoam (Higuera et al. (2014); Alcérreca-Huerta and Oumeraci (2016); Liang and Jeng (2018); Guler et al. (2018)), an extended Forchheimer law which adds a mass term that accelerates a certain amount of water considered.

In this paper, we present a triple-coupled Fluid-Porous-Solid model. The fluid model is described by the Volume-Averaged Reynolds-Averaged Navier-Stokes (VARANS) equations in which the extended Forchheimer law used to calculate the porous medium flow is added to the inertia terms (Hsu et al. (2002)). The solid model, which is based on the Discontinuous Deformation Analysis (DDA) method-a kind of DEM method, is used to compute the movement of the caisson and armour units (Shi (1992)). This method enables to take into account the shapes of armour units, as well as the contact between blocks. The coupling between the fluid and the solid is carried out by a transmission strategy of the fluid mesh nodes' pressure towards the solid polygon vertices, while the coupling between the fluid and the porous medium consists of the equations of the porous model in the terms of the inertia of the fluid model.

The structure of this paper is as follows: In section 2, equations of motion for the fluid and for the solid are introduced. The governing equations of the fluid-porous coupled model and of the DDA method are detailed. A transmission strategy is also given to couple the fluid and solid model. Section 3 is devoted to the validation of fluid and solid models. Simulation results of the flow patterns around the breakwater and the stability of armour units are presented in section 4. Section 5 concludes the paper.

2. Mathematical formulation of the problem

A schematic illustration of the studied problem is shown in Fig. 1. In order to investigate the problem, a numerical approach that couples the Fluid-porous model and the Solid-DDA model is proposed, wherein the fluid model is based on the Volume-Averaged RANS equations, the solid model is based on the DDA method, and the porous model is described by the non-linear Forchheimer model. The governing equations of the models are shown below:

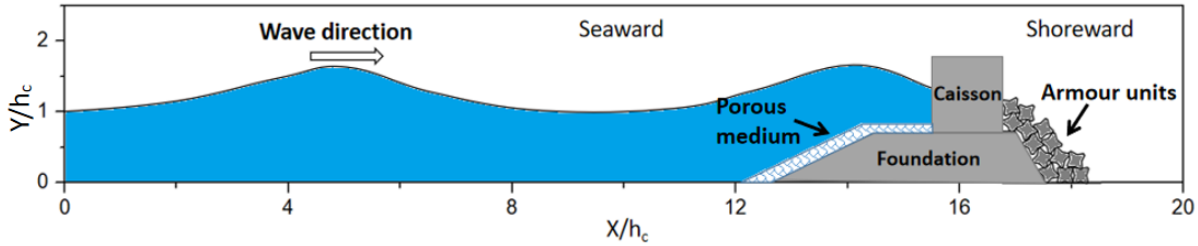

Figure 1: Schematic illustration of the studied problem

2.1. Governing equations of fluid-porous coupled model

2.1.1. RANS equations for turbulence flows

The incompressible turbulence flow around the breakwater are been investigated by the RANS (Reynolds-Averaged Navier–Stokes) equations. The mass and momentum conservation functions are (Ji et al. (2014a)):

$$\nabla \cdot \boldsymbol{U} = 0 \tag{1}$$

$$\frac{\partial \rho \boldsymbol{U}}{\partial t} + \nabla \cdot (\rho \boldsymbol{U}\boldsymbol{U}) = -\nabla P + \boldsymbol{g} \cdot \boldsymbol{X} \nabla \rho + \nabla \mu_{eff} \nabla \boldsymbol{U} + \sigma \kappa \nabla \alpha \tag{2}$$

where $\boldsymbol{U}$ is the velocity vector, $\boldsymbol{X}$ is the Cartesian position vector, $\boldsymbol{g}$ denotes the gravitational acceleration vector, and ρ represents the weighted averaged density. The term $\mu_{eff} = \mu + \mu_t$, where μ is the weighted average dynamic viscosity and the μ_t is the dynamic turbulence viscosity calculated by $k - \epsilon$ model. $\sigma \kappa \nabla \alpha$ signifies the surface tension effects, where σ is the surface tension, α is the fluid volume fraction, and $\kappa = \nabla \frac{\alpha}{|\alpha|}$.

2.1.2. Extended Forchheimer equations for porous medium

Darcy's law has been traditionally used for describing the transport properties of porous media; however, as the flow velocity increases, Darcy's law became inapplicable as the relationship between pressure and velocity becomes non-linear. A correction term (see the second term in Eq.(3)), based on a quadratic velocity, was added by Forchheimer (Whitaker (1996)) to take this non-linearity into account. Furthermore, in the present study, an added mass term C_A (Higuera et al. (2014)) was considered. To accelerate the same volume of water in a porous medium, additional momentum is required(Mèndez et al. (2001)). The extended Forchheimer equation can be written as:

$$P_{porous} = A\boldsymbol{U} + B\boldsymbol{U}|\boldsymbol{U}| + \frac{\rho}{n} C_A \frac{\partial \boldsymbol{U}}{\partial t} \tag{3}$$

where P_{porous} is the porous medium pressure, and the coefficients A and B are (Van Gent (1996); Higuera et al. (2014)) :

$$A = \mu_1 \frac{(1-n)^3}{n^2} \frac{\mu}{D_{50}^2} \tag{4}$$

$$B = \mu_2 (1 + \frac{7.5}{K_C}) \frac{1-n}{n^2} \frac{\rho}{D_{50}} \tag{5}$$

where D_{50} is the mean diameter of the porous material. μ_1 and μ_2 are empirical coefficients related to the linear and nonlinear drag force, respectively. $K_C = \frac{T_o U_M}{n D50}$ is the Keulegan-Carpenter number where U_M is the maximum oscillatory velocity. T_o is the period of the oscillation (Van Gent (1996)).

2.1.3. Volume-averaged RANS equation for coupled fluid-porous

In order to correspond the extended Forchheimer Eq.(3) with the RANS equations, we introduce the volume-averaged velocity $\langle \boldsymbol{U} \rangle$ that exists in the interstices of the solid framework of the porous medium, given by:

$$\langle \boldsymbol{U} \rangle = \frac{1}{V} \int_{V_f} \boldsymbol{U} dV \tag{6}$$

where $\boldsymbol{U}$ is the hydrodynamic velocity with respect to the fluid, V is the total volume, and V_f is the part of V which is occupied by the fluid. In what follows, we set the porosity $n = \frac{V_f}{V}$. Then, by substituting volume-averaged velocity Eq.(6) in the RANS Eqs. (1-2), we obtain the following VARANS equations:

$$\nabla \cdot \langle \boldsymbol{U} \rangle = 0 \tag{7}$$

$$(1 + C_A)\frac{\partial}{\partial t}\frac{\rho \langle \boldsymbol{U} \rangle}{n} + \frac{\rho}{n^2}\langle \boldsymbol{U} \rangle \nabla \langle \boldsymbol{U} \rangle = -\nabla P + \boldsymbol{g}X \cdot \nabla \rho + \frac{1}{n}\nabla \mu_{eff} \nabla \langle \boldsymbol{U} \rangle + \sigma \kappa \nabla \alpha - A\frac{\langle \boldsymbol{U} \rangle}{n} - B|\frac{\langle \boldsymbol{U} \rangle}{n}|\frac{\langle \boldsymbol{U} \rangle}{n} \tag{8}$$

where $C_A = 0.34$ denotes the added mass coefficient, which is kept constant in the present study (Higuera et al. (2014)).

2.1.4. VOF method and numerical procedure

The computational model is built with a two-phase model (Fluid-air) and the free surface that separates these two phases can cut a cell of the computational mesh into two unequal parts. Each part contains a quantity of each phase. In what follows, the Volume-of-Fluid (VOF) method is used to describe the volume fraction of the fluid inside each computational cell which will be transmitted to VARANS. It is based on the following transport equation (Hirt and Nichols (1981)):

$$\frac{\partial \alpha}{\partial t} + \nabla \cdot \alpha \boldsymbol{U} + \nabla \cdot \boldsymbol{U_c} \alpha (1 - \alpha) = 0 \tag{9}$$

where α is the fluid phase fraction laying between 0 and 1, where α=0 corresponds to full of air and α=1 corresponds to full of fluid. However, in order to obtain physical results, there must be some limitations: a clear interface must be maintained, and α must be limited between 0 and 1. Weller (2002) added an artificial compression term $\nabla \cdot \alpha(1-\alpha)$. This method only uses non-zero values at the interface. In addition, $|\boldsymbol{U_c}| = [min(C_\alpha |\boldsymbol{U}|), max(|\boldsymbol{U}|)]$, where the factor C_α can be specified. If $\boldsymbol{U_c}$ is normal to the interface, the fluid will not be compressed, which points to a larger value of α and therefore from the air to the water phase. The boundedness of this equation is achieved by the specially designed solver MULES (multi-dimensional universal limiter for explicit solution).

In the present study, the VARANS models are solved by using the PIMPLE algorithm (pressure implicit with the splitting of operators) to compute the pressure and SIMPLE (semi-implicit method for pressure-linked equations) algorithm to obtain the velocity fields. Its main structure is inherited from the original PISO but allows equations to be relaxed to ensure the convergence of all equations at each time step (Higuera et al. (2014); Cai et al. (2017)).

2.2. Governing equations of the solid model

In order to investigate the movement and the stability of the caisson and armour units, the Discontinuous Deformation Analysis (DDA) method is used. In this method, the displacement at any point (x, y) of a block

i can be described by its first-order approximation (Shi (1992)):

$$\boldsymbol{\chi_i} = \begin{pmatrix} u_i \\ v_i \end{pmatrix} = \boldsymbol{T_i D_i} \tag{10}$$

where $\boldsymbol{T_i} = \begin{pmatrix} 1 & 0 & -(y-y_0) & (x-x_0) & 0 & (y-y_0)/2 \\ 0 & 1 & (x-x_0 & 0 & (y-y_0) & (x-x_0)/2 \end{pmatrix}$ is the transformation matrix, and $\boldsymbol{D_i} = (u_0 \quad v_0 \quad \gamma_0 \quad \varepsilon_{xx} \quad \varepsilon_{yy} \quad \varepsilon_{xy})^T$ is the displacement matrix which is associated with six variables. u_0 and v_0 are the translations of the block gravity center in x and y directions, γ_0 is the rotation around (x_0,y_0), and ε_{xx}, ε_{yy} and ε_{xy} are the normal and shear strains.

Based on the relationship between the strain and the displacement for block i, we have:

$$\boldsymbol{\varepsilon} = \begin{pmatrix} \frac{\partial}{\partial x} & 0 \\ 0 & \frac{\partial}{\partial y} \\ \frac{1}{2}\frac{\partial}{\partial y} & \frac{1}{2}\frac{\partial}{\partial x} \end{pmatrix} \begin{pmatrix} u \\ v \end{pmatrix} = \boldsymbol{L\chi} \tag{11}$$

where $\boldsymbol{L}$ is the differential operator matrix for a 2D problem.

Here, we assume that the deformation is elastic and linear. Therefore, we get:

$$\boldsymbol{\varepsilon_i} = \boldsymbol{LT_iD_i} = \boldsymbol{BD_i} \tag{12}$$

$$\boldsymbol{\sigma_i} = \boldsymbol{E\varepsilon_i} = \boldsymbol{EBD_i} \tag{13}$$

where $\boldsymbol{E}$ is the elastic matrix (Shi (1992)) and $\boldsymbol{B} = \begin{bmatrix} 0 & 0 & 0 & 1 & 0 & 0 \\ 0 & 0 & 0 & 0 & 1 & 0 \\ 0 & 0 & 0 & 0 & 0 & 1 \end{bmatrix}$.

The total potential energy Π_p of the block i which is the summation of all the potential energy sources, which includes the elastic strain energy, initial stress potential energy, body force potential energy, and inertial energy, is given by:

$$\Pi_p = \int_{A_i} \frac{1}{2}\boldsymbol{\varepsilon_i^T \sigma_i} dA_i + \int_{A_i} \boldsymbol{\varepsilon_i^T \sigma_0} dA_i - \int_{A_i} \boldsymbol{\chi_i^T f}_b dA_i + \int_{A_i} \boldsymbol{\chi_i^T} m \boldsymbol{T}_i \boldsymbol{\ddot{D}_i} dA_i \tag{14}$$

where $\boldsymbol{f_b}$ is the body forces applied on a block i, m is the block mass per unit area and $\boldsymbol{\sigma_0}$ is the initial stress.

Substituting Eq. (10),(12) and (13) into Eq. (14), the total potential energy of a system of N blocks is expressed as:

$$\Pi_p = \sum_{i=1}^{N} \left(\boldsymbol{D}_i^T \boldsymbol{M\ddot{D}_i} + \frac{1}{2}\boldsymbol{D_i^T K D_i} - \boldsymbol{D_i^T F} \right) \tag{15}$$

where $\boldsymbol{M}$=$\int_{A_i} m\boldsymbol{T_i^T T_i} dA_i$ is the mass matrix, $\boldsymbol{K}$= $\int_{A_i} \boldsymbol{B}^T \boldsymbol{EB} dA_i$ is the stiffness matrix, and $\boldsymbol{F} = \int_{A_i} (\boldsymbol{T_i^T f_b} - \boldsymbol{B}^T \boldsymbol{\sigma}_0) dA_i$ is the external forces matrix. By minimizing the potential energy, we obtain:

$$\frac{\partial \Pi_p}{\partial \boldsymbol{D_i^T}} = 0 \Rightarrow \boldsymbol{M\ddot{D}} + \boldsymbol{KD} = \boldsymbol{F} \tag{16}$$

Then, the displacement and the velocity in Eq. (16) can be approximated by the Newmark$-\beta$ method:

$$\begin{aligned} \boldsymbol{D}_{n+1} &= \boldsymbol{D}_n + \Delta t \boldsymbol{\dot{D}}_n + \frac{\Delta t^2}{2}\left[(1-2\beta_1)\boldsymbol{\ddot{D}}_n + 2\beta_1 \boldsymbol{\ddot{D}}_{n+1}\right] \\ \boldsymbol{\dot{D}}_{n+1} &= \boldsymbol{\dot{D}}_n + \Delta t \left[(1-\beta_2)\boldsymbol{\ddot{D}}_n + \beta_2 \boldsymbol{\ddot{D}}_{n+1}\right] \end{aligned} \tag{17}$$

where $\ddot{\boldsymbol{D}}$ and $\dot{\boldsymbol{D}}$ are the acceleration and velocity matrices, respectively, and $\beta_1 = 1/2$ and $\beta_2 = 1$ for the implicit scheme (Ding et al. (2020). Substituting Eq. (17) into Eq. (16)), we obtain:

$$(\boldsymbol{K} + \frac{2\boldsymbol{M}}{\Delta t^2})\boldsymbol{D}_{n+1} = \boldsymbol{F} + \frac{2\boldsymbol{M}}{\Delta t}\dot{\boldsymbol{D}}_n \tag{18}$$

And then the compact form is given by:

$$\hat{\boldsymbol{K}}\boldsymbol{D} = \hat{\boldsymbol{F}} \tag{19}$$

Consequently, we get the global matrix:

$$\begin{pmatrix} \hat{\boldsymbol{K}}_{11} & \hat{\boldsymbol{K}}_{12} & \hat{\boldsymbol{K}}_{13} & \dots & \hat{\boldsymbol{K}}_{1n} \\ \hat{\boldsymbol{K}}_{21} & \hat{\boldsymbol{K}}_{22} & \hat{\boldsymbol{K}}_{23} & \dots & \hat{\boldsymbol{K}}_{2n} \\ \hat{\boldsymbol{K}}_{31} & \hat{\boldsymbol{K}}_{32} & \hat{\boldsymbol{K}}_{33} & \dots & \hat{\boldsymbol{K}}_{3n} \\ \vdots & \vdots & \vdots & \vdots & \vdots \\ \hat{\boldsymbol{K}}_{n1} & \hat{\boldsymbol{K}}_{n2} & \hat{\boldsymbol{K}}_{n3} & \dots & \hat{\boldsymbol{K}}_{nn} \end{pmatrix} \begin{pmatrix} \boldsymbol{D}_1 \\ \boldsymbol{D}_2 \\ \boldsymbol{D}_3 \\ \vdots \\ \boldsymbol{D}_n \end{pmatrix} = \begin{pmatrix} \hat{\boldsymbol{F}}_1 \\ \hat{\boldsymbol{F}}_2 \\ \hat{\boldsymbol{F}}_3 \\ \vdots \\ \hat{\boldsymbol{F}}_n \end{pmatrix} \tag{20}$$

where $\hat{\boldsymbol{F}}_i$ and $\boldsymbol{D}_i$ are the sub-matrices of force and displacement, which are 6×1 sub-matrices. The $\hat{\boldsymbol{K}}_{ij}$ are 6×6 sub-matrices. Sub-matrices $\hat{\boldsymbol{K}}_{ij}$ $(i = j)$ are determined by the block material properties, whereas $\hat{\boldsymbol{K}}_{ij}$ $(i \neq j)$ are related to the contacts between blocks.

It should be noted that when the contact between the blocks takes place, the associated potential energy must be added to the global equilibrium equation (Eq. (15)), and then the associated contact sub-matrices have to be added to the global matrix Eq. (20). In the present study, the surface contact constraints of blocks are enforced by the penalty method. Taking the contact of two blocks i and j as an example, where the penetration distance of point P_1 into edge P_2P_3 of block j is δ. Using the penalty method is equivalent to placing a spring between the two blocks, as shown in Fig. 2.

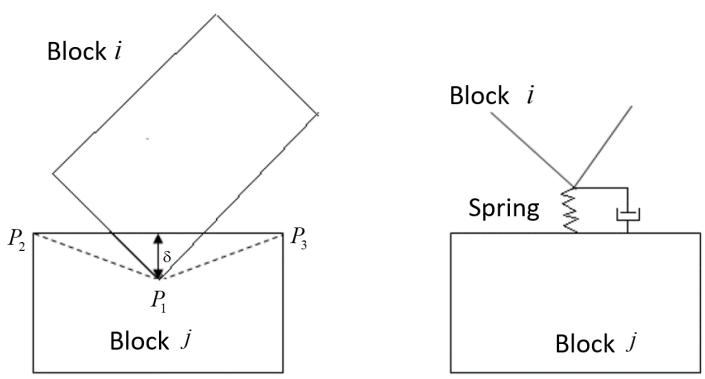

Figure 2: Interaction between two contacting blocks

The strain energy of the contact spring reads:

$$\Pi_c = \frac{1}{2}P\delta^2 \tag{21}$$

where P is the coefficient of penalty which can vary between 10E and 1000E, where E denotes Young's modulus (Shi (1992)). The block kinematics of the DDA method are obtained by the open-close iteration which is adding or removing a stiff spring in each time step at the contact position where tension and interpenetration do not exist.

2.3. Coupling procedure of Fluid-Solid interaction

The coupling between the fluid and the solid models requires a transfer of data from one model to another. In our case, the fluid model uses meshes while the solid model is meshless (see Fig. 3 (a)) since it is based on the DDA method. Therefore, an adequate data transfer strategy is required in order to faithfully reproduce the studied physical phenomena (Kaidi et al. (2012)). It consists in converting the nodal pressure forces of the fluid (f_i, f_j) into equivalent forces F_i at the vertex points of the solid (see Fig. 3 (b)-(c) and Eq. (23)). It is specified that in this fluid-solid coupling, the transfer is retroactive, where the fluid transfers to the solid the pressure force, a force considered external to the solid.

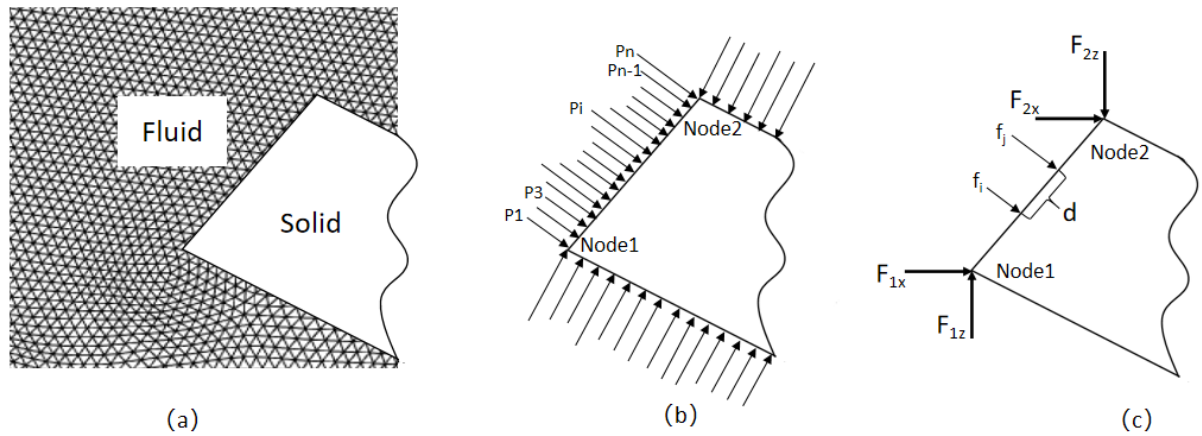

Figure 3: Fluid/solid interface:(a) fluid finite element mesh and solid; (b) fluid pressures in the mesh points (c) conversion of fluid pressures into equivalent vertex forces

$$f_i = p_i \frac{d}{2}; f_j = p_j \frac{d}{2} \tag{22}$$

where p_i and p_j are the fluid pressures at nodes i and j, and d is the distance of the finite element edge from node i to node j. Finally, the global forces (F_1, F_2) acting on the DDA block can be written as:

$$\begin{aligned} F_{1x} &= \sum_{i=1}^{n} f_i n_x \left(\frac{d_2}{d_1+d_2}\right), \quad F_{1y} = \sum_{i=1}^{n} f_i n_z \left(\frac{d_2}{d_1+d_2}\right) \\ F_{2x} &= \sum_{i=1}^{n} f_i n_x \left(\frac{d_1}{d_1+d_2}\right), \quad F_{2y} = \sum_{i=1}^{n} f_i n_z \left(\frac{d_1}{d_1+d_2}\right) \end{aligned} \tag{23}$$

where n is the total number of nodes in the edge, d_1 and d_2 are the distances from the given node to vertices 1 and 2, and n_x and n_y represent the directions along x and y respectively.

A flowchart of procedures and connections between the coupled fluid-porous-solid models, including boundaries, inputs and outputs of each model, has been created as previously described, and is shown in Fig. 4.

3. Numerical model and validation

The numerical simulations were performed to analyze the flow evolution and to characterize the forces on the breakwater subjected to violent wave impacts. The breakwater is composed of a vertical caisson

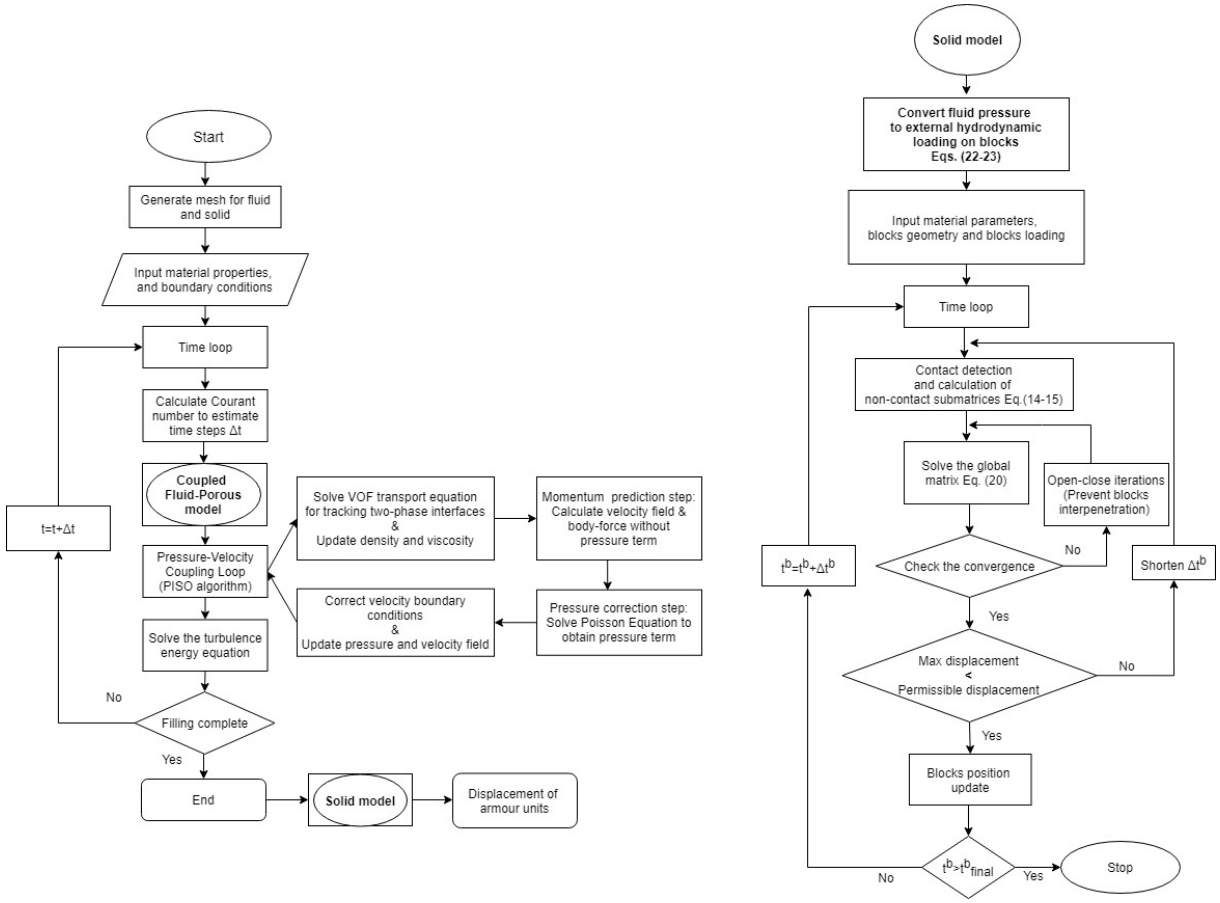

Figure 4: Flow chart of modeling procedure.

with shoreward armour units and a porous seaward armour layer (see Fig. 5). The hydrodynamic impact is generated by the solitary wave, with a wave height (h_w=6 m) and a water depth d_w=10 m. The caisson position x/h_c= 15.96 (where h_c=13 m is the height of the caisson)(Fang et al. (2015); Martin-Medina et al. (2018)). It is worth noting that the armour layer protects the structure from the attacks of incident waves by dissipating their energy. These armour layers are often built of large armour units and can be considered as a porous medium. Indeed, many recent scientific studies have considered the porosity parameter to represent different types of armour units in the CFD simulations. Van Gent (1996) proposed a value laying between 0.25 to 0.4 for cube-shaped units and suggested a porosity value of 0.49 for tetrapod-shaped units. An armour layer thickness of 2 m and a porosity value of 0.49 are used in the following simulations. The location of the gauges is also identified in Fig. 5, numbered from 1 to 5, to monitor the surface and the velocity of waves.

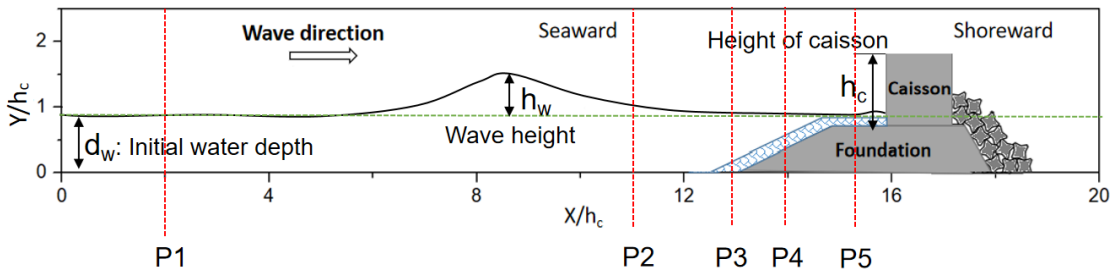

Figure 5: Schematic illustration of the computational domain. Wave type: solitary wave; wave height h_w=6 m; water depth d_w = 10m; armour layer thickness T_a=2 m; breakwater caisson height h_c=13 m; caisson position: x/h_c=15.96. The precise location of gauges P1-P5 is 2h_c, 11h_c, 13h_c, 14h_c and 15.5h_c (m), respectively.

3.1. Boundary conditions

- In the input computational domain, the free surface elevation η is given by:

$$\eta = h_w sech^2 \left[\sqrt{\frac{3h_w}{4d_w^3}} X + \psi \right] \tag{24}$$

where $X = (x - ct)$, h_w is the wave height, d_w is the water depth, ψ is the wave phase shift, and the wave celerity c is $\sqrt{g(h_w + d_w)}$. The horizontal and vertical velocity components U_h and U_v verify (Lee et al. (1982)):

$$U_h = \frac{\eta\sqrt{gd_w}}{d_w} \left[1 - \frac{\eta}{4d_w} + \frac{d_w^2}{3\eta} \left(1 - \frac{3y^2}{2d_w^2} \right) \frac{d^2\eta}{dX^2} \right] \tag{25}$$

and

$$U_v = \frac{-y\sqrt{gd_w}}{d_w} \left[\left(1 - \frac{\eta}{2d_w} \right) \frac{d\eta}{dX} + \frac{1}{3} d_w^2 \left(1 - \frac{y^2}{2d_w^2} \right) \frac{d^3\eta}{dX^3} \right] \tag{26}$$

where x and y are the horizontal and the vertical space variables. Here, we assume that the boundary is at x= 0, and the free surface will start from the highest point of the solitary wave.

- At the top boundary, we assume $p = p_{atmospheric}$; at the bottom boundary, we set a slip condition, where the roughness can be assumed to be negligible.

3.2. Mesh and time step convergence

The validation of the fluid model is carried out by comparing the calculated horizontal velocity and water height with the theoretical free surface elevation η at transect P1 (see Fig.5) deduced from Eq. (24). Three types of meshes are used for mesh convergence validation, which contain 24510, 48000 and 94080 tetrahedral mesh elements, respectively. A refinement ratio $\sqrt{2}$ is used for the mesh validation (Ji et al. (2014b)). The grid spacing of the coarser meshes $(\Delta x_c, \Delta y_c)$ to grid spacing of the finer meshes $(\Delta x_f, \Delta y_f)$ is given as:

$$r_g = \frac{\Delta x_c}{\Delta x_f} = \frac{\Delta y_c}{\Delta y_f} = \sqrt{2} \tag{27}$$

Fig. 6(1) shows that the fine and medium meshes have similar results and give better than coarse mesh. Considering both the accuracy and the simulation time, the medium mesh is used for the following studies. Three time steps are designed. Fig. 6 (2) shows that the results of the three time step cases are all reasonable. The accuracy of the case (Δt=0.1 s) is clearly enough; therefore, we use time steps of 0.1 s in this work. The refinement of the space or time steps can improve the quality of the results; however this is not enough. It is therefore necessary to use digital diagrams or models, such as Serre (Do Carmo et al. (2018, 2019)) or Extended Boussinesq-like models (Ouahsine et al. (2013)), which have good dispersive capacities for accurate prediction of wave activity.

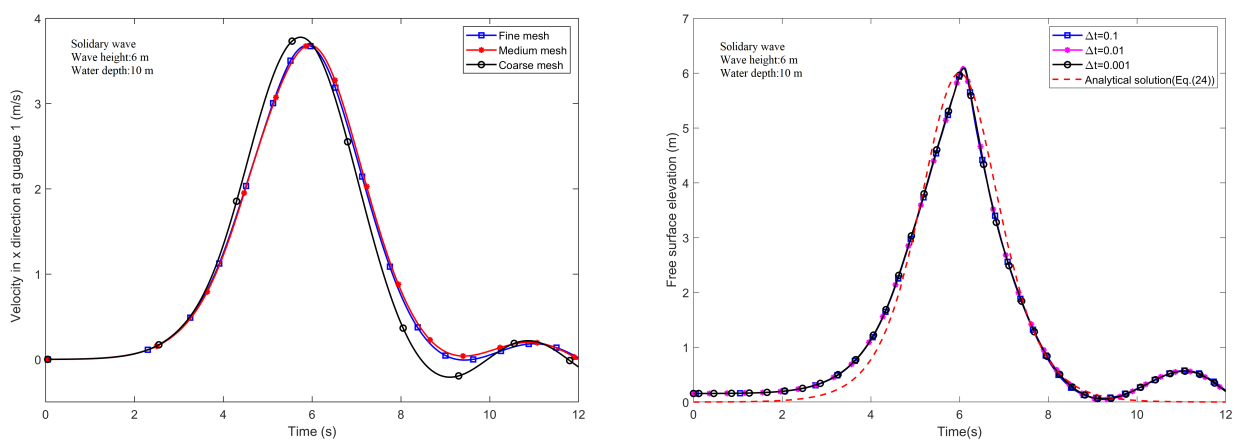

(a) (b)

Figure 6: (a) Horizontal velocity and free surface elevation of mesh, and (b) time step convergence at gauge P1 (see Fig. Fig. 5 for the wave parameters and gauges location).

3.3. Solid model validation

The validation of the solid model is carried out by comparing the DDA numerical results with both the experimental and the numerical results given by Komodromos et al. (2008). Thus, the behavior of seven 48 $mm \times 48\ mm \times 29\ mm$ blocks with a mass of 135.5 g under harmonic excitations (at the base) is simulated by DDA wherein we assume that the contact stiffness is $10^7 N/m$ and friction angle ϕ is 34°, and the peak ground accelerations is 2.15 m/s^2. For four different frequencies, the computed results are compared with the experimental observations. The DDA simulations show similar responses to experimental observations, as shown in Fig. 7. Furthermore, compared to the DEM results, the DDA results have higher accuracy.

For four different frequencies, the acceleration ($a_{initiate}$) to initiate the rocking or sliding is calculated by the DDA model. The results from the experimental have a great agreement with the numerical simulations, as shown in Fig. 8. Therefore, the DDA can be used to investigate the displacement of the vertical caisson and the discrete rear structures.

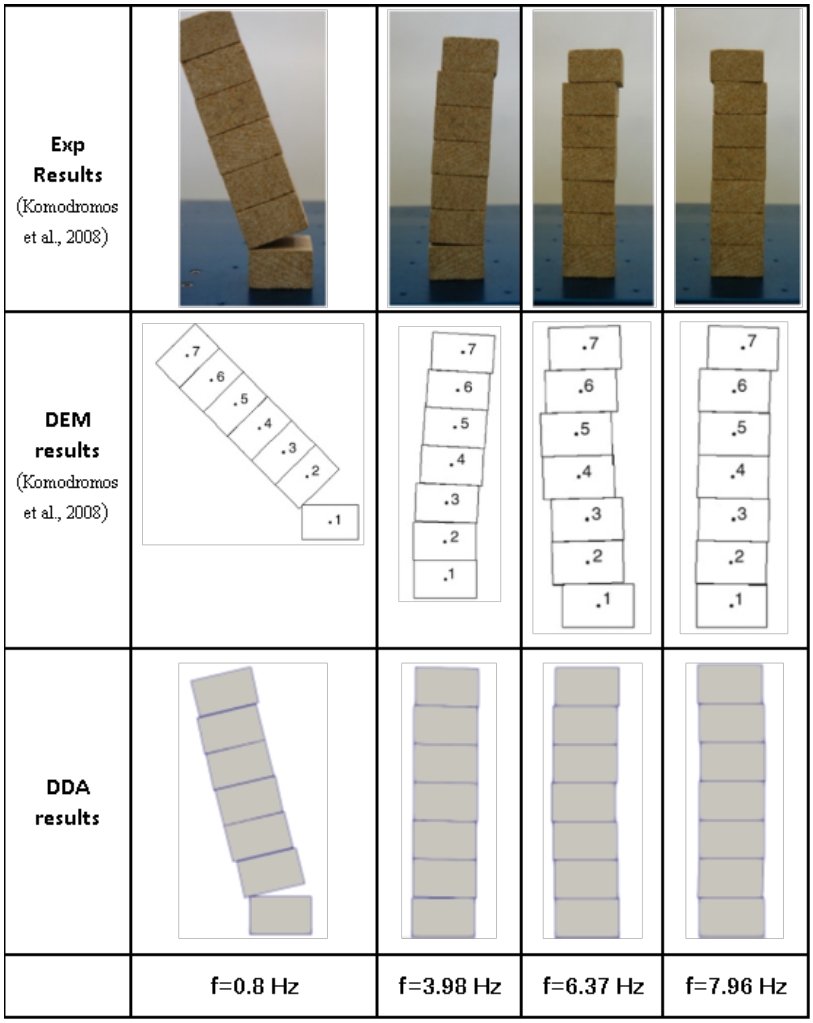

Figure 7: Comparison between the experimental results (Komodromos et al. (2008)) and the numerical results computed by DEM and DDA. The dimension of one block is 48 mm ×48 mm ×29 mm, the mass is 135.5 g, the contact stiffness is $10^7 N/m$, the friction angle is $\phi = 34^o$, and the peak ground accelerations is 2.15 m/s^2

.

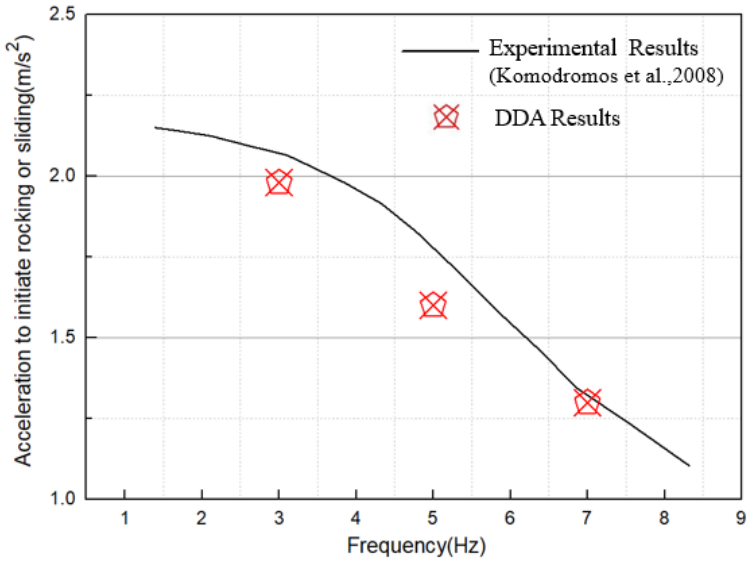

Figure 8: Comparison between the experimental values of $a_{initiate}$ (Komodromos et al. (2008)) and DDA results.

4. Simulation results

4.1. Flow patterns around the breakwater

The simulation of the flow patterns around the breakwater was done by considering the fluid-porous coupling. The wave evolution around the breakwater presented in Fig. 9 shows that as the wave approaches the vertical caisson grows considerably in amplitude until the breaking process occurs (Fig. 9(b)). This then leads to an up-moving jet due to the wave-squeezing processes (Fig. 9(c)).

The distribution of the wave pressure in front of the vertical caisson is shown in Fig. 10. The normal pressure due to solitary waves is mainly located between 20 s and 25 s. The results show that the fluid pressure is relatively high in the lower half of the caisson, which can induce a risk of sliding of the structure or even give rise to a liftforce which could accentuate the overturning process since the maximum pressure is located at the caisson's toe (see point A, Fig. 10).

At the vicinity of the breakwater, the height of the waves (expressed as H=$\eta + d_w$) increases considerably as they approach the breakwater until the breaking process occurs, as shown in Fig. 11. The wave-breaking process happens after the impact between the wave and the caisson (Ouahsine et al. (2013)). Three main reasons cause this wave-breaking process:(1) non-linear terms and secondary waves, (2) reflection on the porous medium and the caisson, (3) wave-wave interactions.

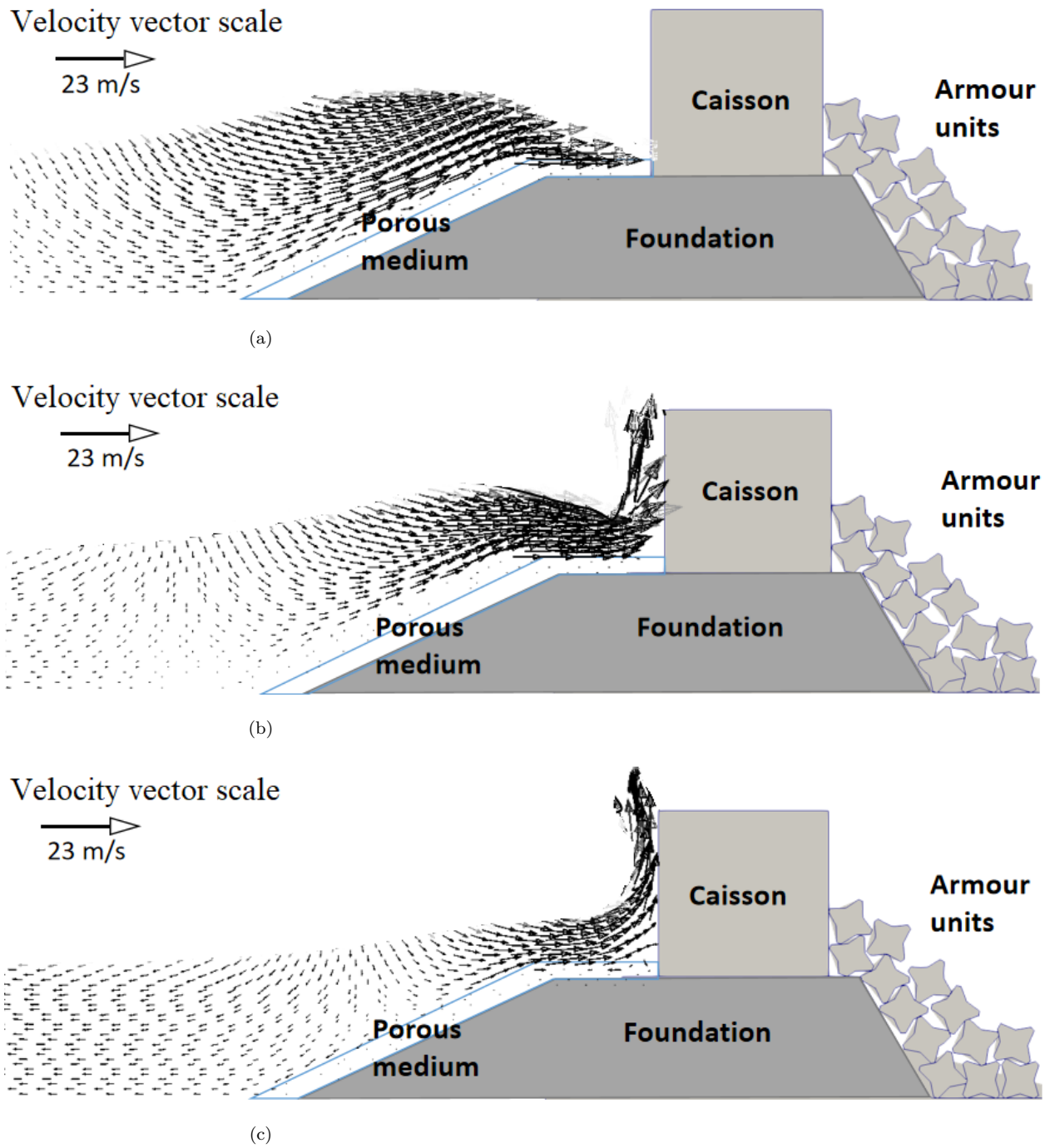

Figure 9: Pattern changes: (a) t=19.5 s; (b) t=20.5 s; (c) t=21.5 s. The impacting wave is a solitary wave with a wave height 6 m and a water height 10 m. The caisson height is 13 m. The thickness of the porous medium (porosity = 0.49) is 2 m. The slope is 1:2.

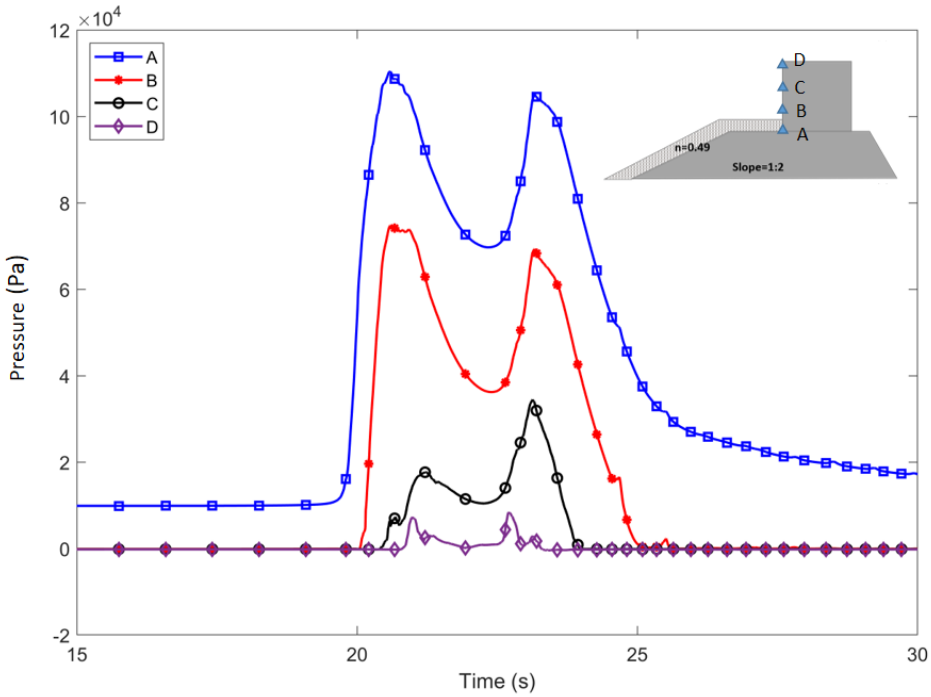

Figure 10: Pressure distribution along the vertical caisson. The impacting wave is a solitary wave with a wave height 6 m and a water height 10 m. Point A is located at the bottom of the caisson. Points B-D are $\frac{1}{3}h_c$, $\frac{2}{3}h_c$, and h_c away from point A.

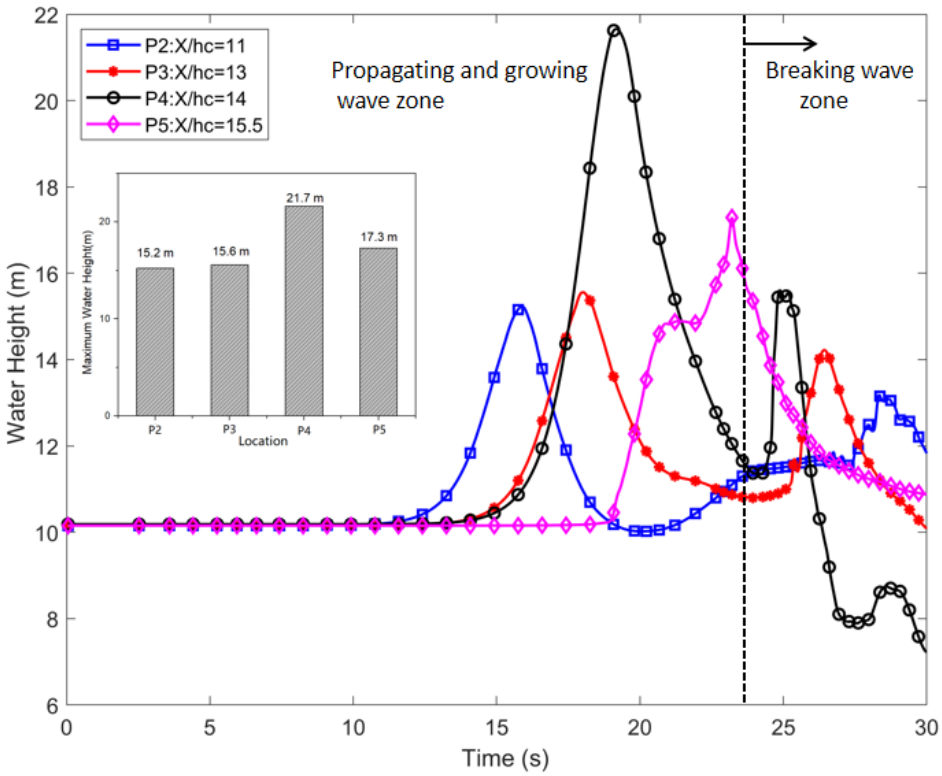

Figure 11: Water height evaluation at the vicinity of breakwater (see Fig. 5)

4.2. Solution behavior with the breakwater seaward slopes

The wave motion and the flow pattern on the breakwater seaward slope are simulated by the Fluid-Porous model, in which four slopes are considered. The slopes are assumed to be 1:S, where S is the ratio of the slope bottom length to the slope height, which equals 1, 2, 3, and 4. The simulation results are shown in Fig. 12.

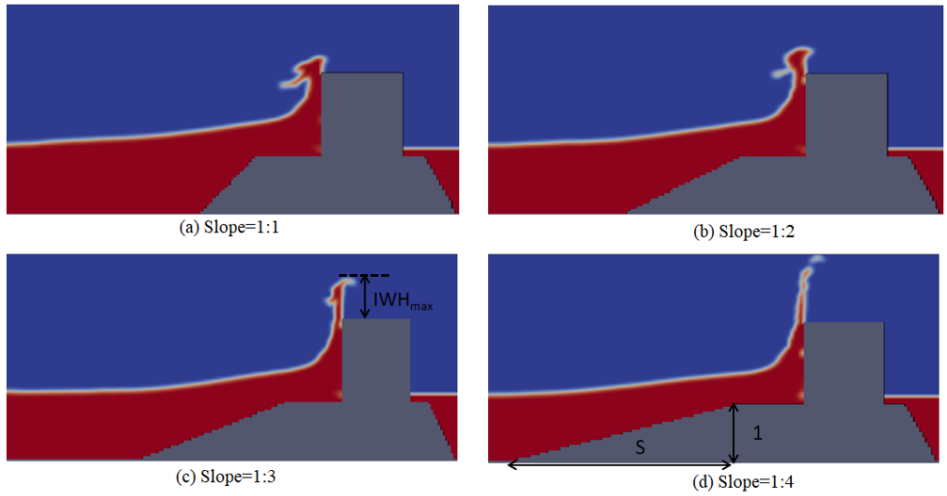

Figure 12: Surface wave deviation with various seaward slopes (1:S). For the wave parameters, see Fig. 5. The IWH$_{max}$ of the four slopes are: (a) 1.86 m,(b) 3.71 m,(c) 5.57 m and (d) 9.28 m, respectively.

We then define the maximum impacting wave height (IWH$_{max}$) as the peak of the incoming wave height after it impacts the caisson, as shown in Fig. 12. Due to the squeezing process of the breakwater, we observe that a larger S induces a bigger (IWH$_{max}$) but less water is ejected. Hence, the Impacting Wave Height (IWH$_{max}$) can be fitted through the following formula:

$$IWH_{max} = \alpha_1 + \alpha_2 e^{\alpha_3 S} \tag{28}$$

where α_1=0.41, α_2=1.45 and α_3=0.5. Fitting results are shown in Fig. 13.

The seaward porous medium affects the wave. The turbulent kinetic energy K for various thickness of the porous layer is shown in Fig. 14. The large porous layer has less turbulent kinetic energy due to a large dissipation. Several turbulences can be found on the upper side of the caisson on the shoreward side, in the middle of caisson on the seaward side, as well as at the top and bottom of the porous medium. The flow in the porous medium initially coincides with the direction of the wave and then opposes it (Van der Meer et al. (2016)). The porous medium significantly reduces the effects of the breaking waves.

4.3. Solution behavior with the shape of shoreward armour units

In order to analyze the stability of the shoreward armour units and the influence of their shape, three typically shaped armour (Kaidi et al. (2012))(see Fig. 15) are modeled and placed on the shoreward side of the breakwater. The armour units are optimally arranged to ensure the initial position stability. Six units, numbered from 1 to 6, are shown in Fig. 16. The breakwater is then subjected to a violent solitary wave

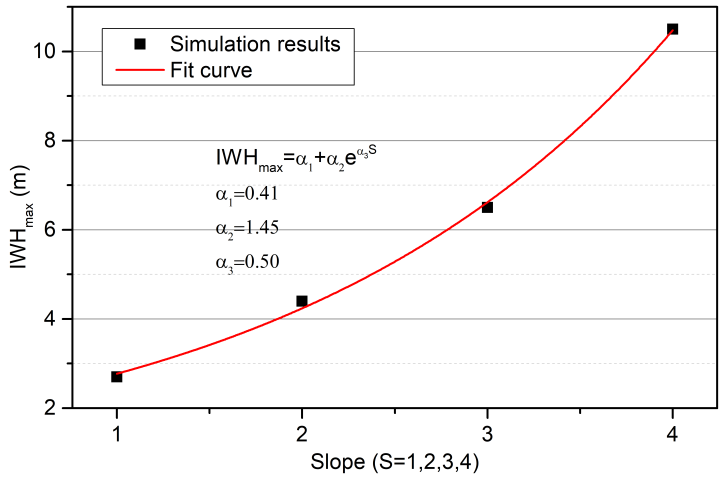

Figure 13: Variation of IWH$_{max}$ (see Fig. 12) for various seaward slopes.

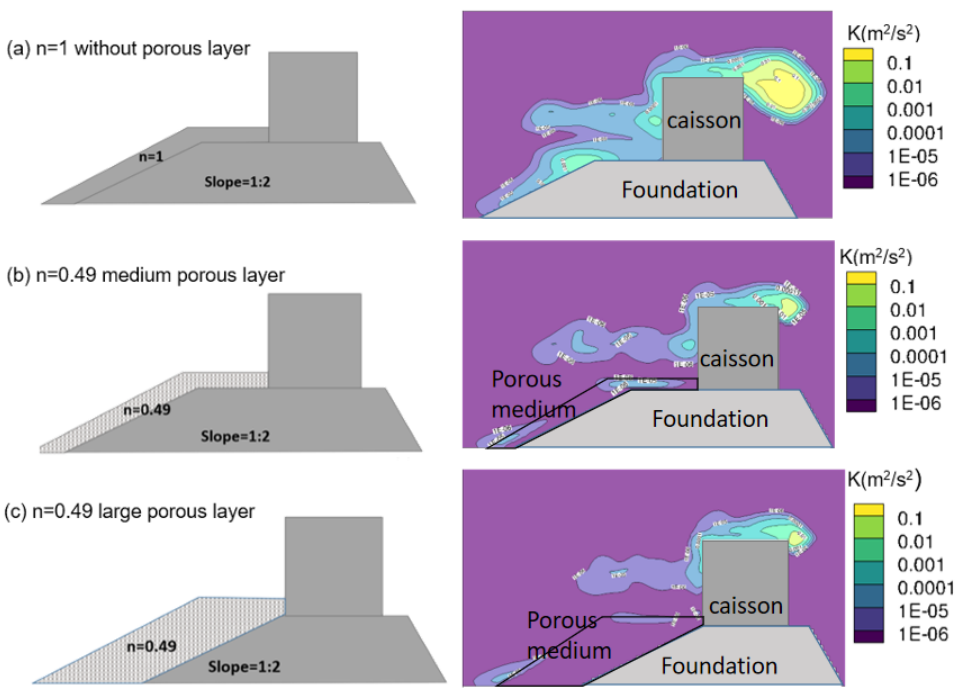

Figure 14: Turbulent kinetic energy K for various porous layer thickness in t=24.0 s. (see Fig. 5 for the wave parameters).

Table 1: Material parameters used for simulations

Young's modulus E	Poisson's ratio ρ	unit weight m	Penalty spring constant P	Coefficient of friction μ
50 GPa	0.30	2400 kg/m^3	2×10^8 N/m	0.6

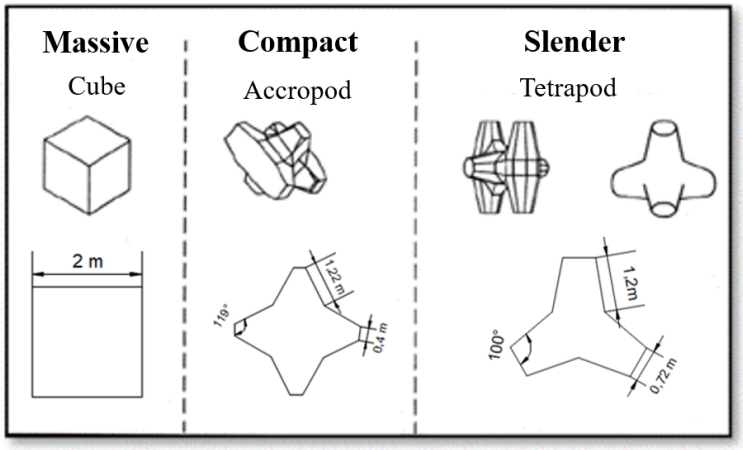

Figure 15: Shapes of armour units used in the simulation.

impact whose input external force is calculated by Eq. (23) ((see the flow in Figs. 9 and 10). The material parameters used for the Solid-DDA model are shown in Table 1.

Fig. 16 shows the initial and the final position of the three various shapes of armour units. The displacement of the caisson hindered by armour units is almost zero and stable while varying degrees of sliding and rotating happen on the armour units. The cubic units are more unstable than the other two; in fact, cubic unit No.2 experienced a significant fall. We found that units No.2 and No.3 have larger vertical displacement while units No.3 and No.6 have large horizontal displacement. Therefore, a falling process always happens on the rear side of the caisson and a sliding process happens on the toe of the breakwater structure. As for the displacement, the accropod and the tetrapod units followed the cubic units in that there is no significant drop; however, the rotation of the units can be seen. Because the two shaped units are under force, the armour units move to rearrange and the structure becomes more stable, with the tetrapod units.

The standard deviation (SD) of the displacement or the rotation of the armour units is used to describe the stability of the breakwater, which is calculated by:

$$SD = \sqrt{\frac{\sum_{i=1}^{N}(\phi_i - \bar{\phi})^2}{N}} \tag{29}$$

where ϕ_i denotes the displacement or rotation value of units i at the final position, $\bar{\phi}$ is the average displacement or rotation value, and $N = 6$. The standard deviations of the horizontal displacement, the vertical displacement, and the rotation are shown in Fig. 17. For the displacement of the armour units, we have obtained $SD_{cube} > SD_{accropod} > SD_{tetrapod}$. For the rotation, however, the accropod units are greater than the cubic and tetrapod units. Furthermore, the cubic units have larger displacements, most of which are in the form of sliding along the slope.

Based on the simulation results, the tetrapod units are the most stable, followed by the accropods, and then by the cubic armour units. The reason is that cubic armour units bring resistance to the breakwater through mass whereas tetrapod and accropod blocks bring resistance through mass and interlock forces among units.

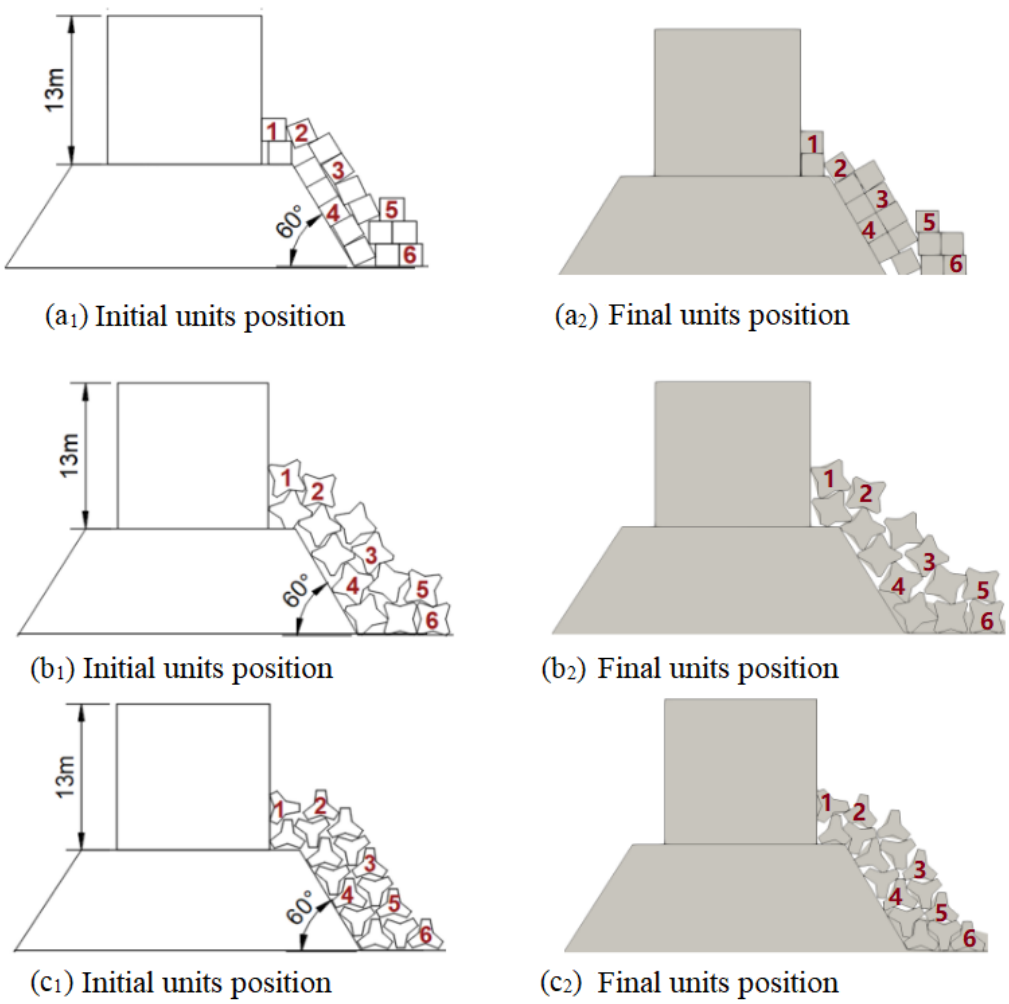

Figure 16: Simulated movement for various shapes of armour units: (a) Cube, (b) Accropod, (c) Tetrapod. The breakwater was subjected to solitary wave impacts whose input external force is calculated by Eq. (23). (See Fig. 5 for the wave parameters).

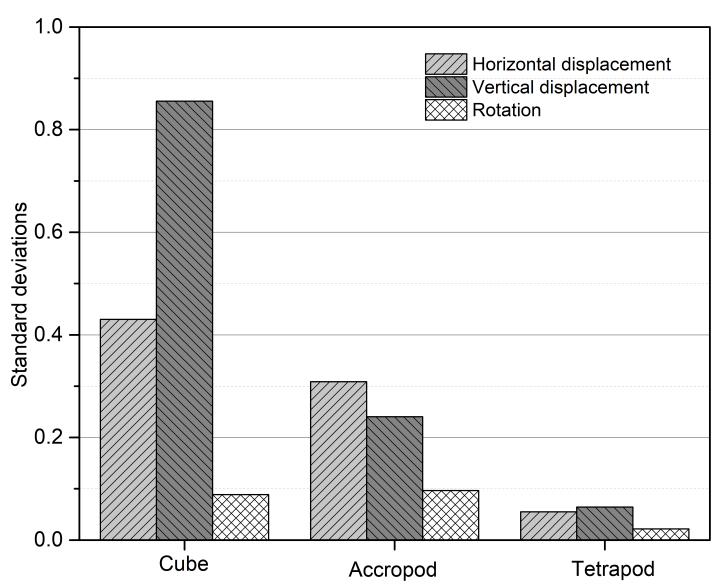

Figure 17: Variation of standard deviations for three shapes of armour units.

4.4. Effect of Cohesion

In this simulation, a cohesion C_f=2 MPa and a tensile strength $\sigma_t = 0.7MPa$ are imposed, which may actually represent concrete placed on the surfaces and contact points. (Kaidi et al. (2012)). These values are obtained by adopting the extended Mohr-Coulomb failure criterion based on the tension cut-off. It consists in reducing the tensile strength of the material by imposing a value of σ_t while ensuring the following condition: $\sigma_t \leq Ccotan\phi$. Thus, by fixing $\sigma_t = 0.7MPa$, we decrease the value of C to C_f, which corresponds to the movement of one block of the caisson. C_f is considered optimal.

Fig. 18 shows that the displacement of the armour units without cohesion is bigger than the units with cohesion. All the units behind the caisson have been moved but the units No.2 and 5 have moved significantly. Therefore, we have chosen to present only the movements of units No.2 and No.5 as shown in Fig. 19. For unit No.2, when cohesion forces work, the steady-state can be reached in about 22.0 s and the maximum displacement is 1.2 m which is far less than 1.90 m without cohesion. For unit No.5, it reaches steady-state at 22.0 s (with cohesion) and 24.0 s (without cohesion). In total, the displacement of the two units was lower by 36.8% and 23.8% respectively, as compared to when cohesion is absent. Therefore, we conclude that cohesion enforces the stability of the breakwater.

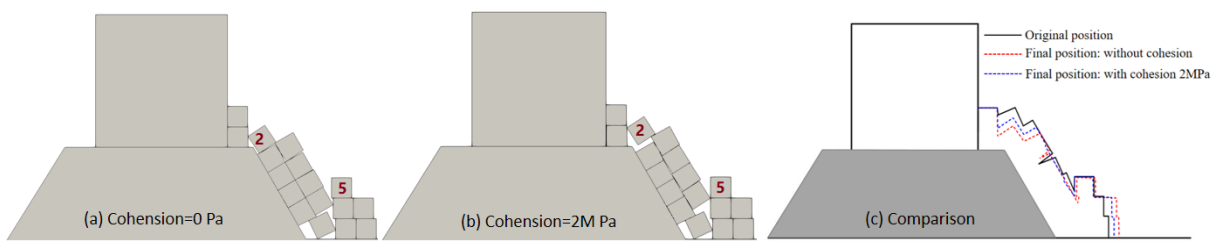

Figure 18: Comparison of the motion of cubic units at final position: (a) cohesion=0 Pa, tensile strength $\sigma_t = 0.7MPa$; (b) cohesion= 2 MPa, tensile strength $\sigma_t = 0.7MPa$; (c) Comparison of the effect of cohesion. The breakwater was subjected to solitary wave impacts whose external force is calculated by Eq. (23) (See Fig. 5 for the wave parameters).

5. Conclusions

This paper presents a fluid-porous-solid triple coupled model to simulate the stability of a caisson-type breakwater. The fluid model is described by the Volume-Averaged Reynolds-Averaged Navier-Stokes (VARANS) equations in which the nonlinear Forchheimer equations for the porous medium are implemented as the terms of inertia. The solid model is based on the DDA method to take the discrete behavior of armor units into account. The coupling between the fluid and the solid is carried out by a transmission strategy of the fluid mesh nodes' pressure towards the solid polygon vertices.

The results of the numerical simulation show that the porosity and the thickness of the porous layer have a significant influence on the distribution of the kinetic energy of turbulence (TKE) around the structure of the breakwater. The greater the thickness, the lower the intensity of the TKE. Indeed, the porous layer, located just in front of the caisson, acts as a support structure that effectively dissipates and absorbs the turbulent kinetic energy of the impacting waves. It reduces the growth of wave crests and the overtopping

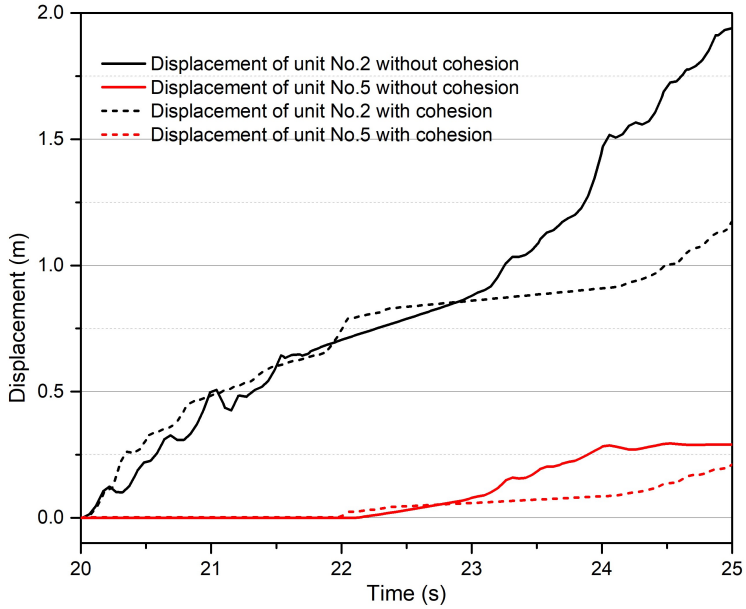

Figure 19: Displacement of cubic armour units 2 and 5 with and without cohesion

of the caisson and also allows slope adjustment just in front of the caisson to avoid possible progressive or severe raveling of the lower part of the structure. The results of the numerical simulations also show that the maximum impacting wave height depends on the slope of the structure of the breakwater. Thus, a new formula has been established for this purpose. Moreover, the results also show that the shape of the armour units is a major factor to be taken into account in the study of the stability of the structure. In particular, they show that tetrapod-shaped units are the most stable, followed by acropod-shaped units and then by cubic-shaped units, and that cohesion enforces the stability of the breakwater.

Acknowledgments

The authors wish to thank the financial support from the China Scholarship Council (CSC).

References

Alcérreca-Huerta, J.C., Oumeraci, H., 2016. Wave-induced pressures in porous bonded revetments. part i: Pressures on the revetment. Coastal Engineering 110, 87–101.

Cai, S.G., Ouahsine, A., Favier, J., Hoarau, Y., 2017. Moving immersed boundary method. International Journal for Numerical Methods in Fluids 85, 288–323.

Cuomo, G., Allsop, W., Bruce, T., Pearson, J., 2010. Breaking wave loads at vertical seawalls and breakwaters. Coastal Engineering 57, 424–439.

Ding, D., Ouahsine, A., Xiao, W., Du, P., 2020. Numerical study of ballast-flight caused by dropping snow/ice blocks in high-speed railways using Discontinuous Deformation Analysis (DDA). Transportation Geotechnics 22, 100314.

Do Carmo, J.A., Ferreira, J., Pinto, L., 2019. On the accurate simulation of nearshore and dam break problems involving dispersive breaking waves. Wave Motion 85, 125–143.

Do Carmo, J.A., Ferreira, J., Pinto, L., Romanazzi, G., 2018. An improved serre model: Efficient simulation and comparative evaluation. Applied Mathematical Modelling 56, 404–423.

Doan, N.S., Huh, J., Mac, V.H., Kim, D., Kwak, K., et al., 2020. Probabilistic risk evaluation for overall stability of composite caisson breakwaters in Korea. Journal of Marine Science and Engineering 8, 148.

Elchahal, G., Younes, R., Lafon, P., 2008. The effects of reflection coefficient of the harbour sidewall on the performance of floating breakwaters. Ocean Engineering 35, 1102–1112.

Fang, K., et al., 2015. A central numerical scheme to 1D Green-Naghdi wave equations. Journal of Applied Mathematics and Physics 3, 1032–1037.

Guler, H.G., Baykal, C., Arikawa, T., Yalciner, A.C., 2018. Numerical assessment of tsunami attack on a rubble mound breakwater using openfoam®. Applied Ocean Research 72, 76–91.

Higuera, P., Lara, J.L., Losada, I.J., 2014. Three-dimensional interaction of waves and porous coastal structures using OpenFOAM®. part i: Formulation and validation. Coastal Engineering 83, 243–258.

Hirt, C.W., Nichols, B.D., 1981. Volume of fluid (VOF) method for the dynamics of free boundaries. Journal of computational physics 39, 201–225.

Hofland, B., Kaminski, M., Wolters, G., 2010. Large scale wave impacts on a vertical wall. Coastal Engineering Proceedings 1, 15.

Hsu, T.J., Sakakiyama, T., Liu, P.L.F., 2002. A numerical model for wave motions and turbulence flows in front of a composite breakwater. Coastal Engineering 46, 25–50.

Ji, S., Ouahsine, A., Smaoui, H., Sergent, P., 2014a. 3D modeling of sediment movement by ships-generated wakes in confined shipping channel. International Journal of Sediment Research 29, 49–58.

Ji, S., Ouahsine, A., Smaoui, H., Sergent, P., Jing, G., 2014b. Impacts of ship movement on the sediment transport in shipping channel. Journal of Hydrodynamics 26, 706–714.

Kaidi, S., Rouainia, M., Ouahsine, A., 2012. Stability of breakwaters under hydrodynamic loading using a coupled DDA/FEM approach. Ocean Engineering 55, 62–70.

Kocaman, S., Ozmen-Cagatay, H., 2015. Investigation of dam-break induced shock waves impact on a vertical wall. Journal of Hydrology 525, 1–12.

Komodromos, P., Papaloizou, L., Polycarpou, P., 2008. Simulation of the response of ancient columns under harmonic and earthquake excitations. Engineering Structures 30, 2154–2164.

Latham, J.P., Mindel, J., Xiang, J., Guises, R., Garcia, X., Pain, C., Gorman, G., Piggott, M., Munjiza, A., 2009. Coupled FEM DEM/Fluids for coastal engineers with special reference to armour stability and breakage. Geomechanics and Geoengineering: An International Journal 4, 39–53.

Lee, J.J., Skjelbreia, J.E., Raichlen, F., 1982. Measurmment of velocities in solitary waves. Journal of the Waterway, Port, Coastal and Ocean Division 108, 200–218.

Liang, Z., Jeng, D.S., 2018. A three-dimensional model for the seabed response induced by waves in conjunction with currents in the vicinity of an offshore pipeline using openfoam. International Journal of Ocean and Coastal Engineering 1, 1850004.

Liu, S., Gatin, I., Obhrai, C., Ong, M.C., Jasak, H., 2019. CFD simulations of violent breaking wave impacts on a vertical wall using a two-phase compressible solver. Coastal Engineering 154, 103564.

Martin-Medina, M., Abadie, S., Mokrani, C., Morichon, D., 2018. Numerical simulation of flip-through impacts of variable steepness on a vertical breakwater. Applied Ocean Research 75, 117–131.

Van der Meer, J., Allsop, N., Bruce, T., De Rouck, J., Kortenhaus, A., Pullen, T., Schüttrumpf, H., Troch, P., Zanuttigh, B., 2016. Eurotop, 2016. manual on wave overtopping of sea defences and related structures. an overtopping manual largely based on european research, but for worldwide application. EurOtop, London, UK , 264.

Mèndez, F., Losada, I., Losada, M., 2001. Mean magnitudes induced by regular waves in permeable submerged breakwaters. Journal of Waterway, Port, Coastal, and Ocean Engineering 127, 7–15.

Ouahsine, A., Smaoui, H., Meftah, K., Sergent, P., Sabatier, F., 2013. Numerical study of coastal sandbar migration, by hydro-morphodynamical coupling. Environmental fluid mechanics 13, 169–187.

Oumeraci, H., 1994. Review and analysis of vertical breakwater failures-lessons learned. Coastal engineering 22, 3–29.

Ren, B., Jin, Z., Gao, R., Wang, Y.x., Xu, Z.l., 2014. SPH-DEM modeling of the hydraulic stability of 2D blocks on a slope. Journal of Waterway, Port, Coastal, and Ocean Engineering 140, 04014022.

Shi, G.H., 1992. Discontinuous deformation analysis: a new numerical model for the statics and dynamics of deformable block structures. Engineering computations 9, 157–168.

Takahashi, H., Sassa, S., Morikawa, Y., Takano, D., Maruyama, K., 2014. Stability of caisson-type breakwater foundation under tsunami-induced seepage. Soils and Foundations 54, 789–805.

Takahashi, S., Shimosako, K.i., Kimura, K., Suzuki, K., 2001. Typical failures of composite breakwaters in Japan. Coastal engineering , 1899–1910.

Van Gent, M.R.A., 1996. Wave interaction with permeable coastal structures, in: International Journal of Rock Mechanics and Mining Sciences and Geomechanics Abstracts, p. 277A.

Weller, H., 2002. Derivation, modelling and solution of the conditionally averaged two-phase flow equations. Nabla Ltd, No Technical Report TR/HGW 2, 9.

Whitaker, S., 1996. The Forchheimer equation: a theoretical development. Transport in Porous media 25, 27–61.